Computational Materials Science 189 (2021) 110263

Contents lists available at ScienceDirect

Computational Materials Science

journal homepage: www.elsevier.com/locate/commatsci

Mesoscopic-scale numerical investigation including the influence of scanning strategy on selective laser melting process

Liu Cao

Institute for Systems Rheology, School of Mechanical and Electrical Engineering, Guangzhou University, Guangzhou 510006, Guangdong, China

ARTICLE INFO

Keywords:
Selective laser melting
Scanning strategy
Grain orientation
Pore defect
Surface roughness
Numerical simulation

ABSTRACT

Selective laser melting (SLM) has become one of the most widely used laser additive manufacturing technologies today. However, the proper selection of scanning strategies is still a key concern for SLM production. In order to quantify the influences of different scanning strategies (One-direction, Two-directions, and Pre-sinter) on the SLM process, this paper calculated the spreading powder process based on the open-source discrete element method framework Yade, predicted the SLM mesoscopic molten pool dynamics behavior based on the open-source finite volume method framework OpenFOAM, and established the simulation flow of the SLM multi-layer multi-path forming process. The influences of different scanning strategies on grain orientation, pore defect, and surface roughness were analyzed and verified in comparison with experimental results. It is found that the grain orientation of the current formed layer under scanning strategies One-direction and Pre-sinter was almost the same as that of the previous formed layer, while the grain orientation of the current formed layer under scanning strategy Two-directions was significantly different from that of the previous formed layer. In addition, the porosity and surface roughness under scanning strategy Pre-sinter were lower than those under scanning strategies One-direction and Two-directions. This paper is expected to provide a basis for the selection of scanning strategies in practical SLM production.

1. Introduction

Selective laser melting (SLM) is one of the most widely used laser additive manufacturing technologies at present, using layer-by-layer spreading powder, melting, solidification and stacking to form three-dimensional solid components[1,2]. However, at present, SLM technology still faces many challenges from industrial application, such as excessive residual stress [3] and deformation [4] of SLM parts, which can hardly meet the usage requirements. It has been shown that there is a significant correlation between the selection of scanning strategies and residual stress and deformation [5,6], therefore, it is of great value to study the influence of scanning strategy on the SLM process in order to promote the SLM technology into industrial application.

Numerous experimental studies have been carried out on the influence of scanning strategy on the performance of SLM parts. The main indicators of interest are porosity [7], surface roughness [8], forming accuracy [9], residual stress [10,11], grain size and orientation [12,13], corrosion performance [14], mechanical properties (tensile strength [15,16], yield strength [17,18], elongation [19], friction property [20], and microhardness [21]), and so on. Aboulkhair *et al.* [22] used six scanning strategies (X, 2X, alternating, X&Y 2HS, pre-sinter, and overlap) to form AlSi10Mg alloy powder and analyzed the influence of the scanning strategy on the part density, and found that the density was highest under scanning strategy pre-sintering. Sun *et al.* [23] investigated the influences of three scanning strategies (X-scan, XY-scan, and Rot-scan) on Ni-alloy crystal texture and found that the scanning strategy could change the grain orientation arranged along the forming direction, with ⟨001⟩ favoring scanning strategies XY-scan and Rot-scan, and ⟨101⟩ favoring scanning strategy X-scan. The obtained experimental results [7–23] have been instrumental in gaining a deeper understanding of the mechanisms by which the scanning strategy influences the SLM process.

Numerical simulation, as a quantitative research tool to obtain three-dimensional process information about the object of study, has become a powerful tool for studying the SLM process [24,25]. For the influence of the scanning strategy on the SLM process, the current relevant simulation studies [26–29] are mainly the prediction of temperature and stress distributions under different scanning strategies based on the macroscopic scale. By macroscopic scale, it means that the powder bed (containing metal particles and voids) is considered as a special material, which indirectly describes the temperature, stress and flow field

E-mail address: caoliu@gzhu.edu.cn.

https://doi.org/10.1016/j.commatsci.2020.110263
Received 17 November 2020; Received in revised form 23 December 2020; Accepted 26 December 2020
Available online 10 January 2021

Nomenclature

α_1, α_2	Volume fractions occupied by the metal and gas phases in the element, respectively
t	Time
$\boldsymbol{u}$	Velocity
f_{metal}	Laser energy distribution coefficient
V_{metal}	Metal-phase volume of the element
V_{sum}	Sum of the metal-phase volumes of the elements activated by the laser in the same local horizontal area
q_{laser}	Laser surface energy density
η	Laser absorptivity of the metal
P_{laser}	Laser power
R	Spot radius
x, y	Horizontal coordinates of the center of the element
x_0, y_0	Horizontal coordinates of the center of the spot
v_{laser}	Scanning speed
Q_{laser}	Laser body energy density
Δz	Equivalent dimension of the element, such as the side length of a cube
$\overline{\rho}, \rho_1, \rho_2$	Mixed density, metal density and gas density, respectively
T	Temperature
$\overline{c}_e$, c_1, c_2	Equivalent specific heat capacity[34], metal specific heat capacity and gas specific heat capacity, respectively
$\overline{k}$	Mixed thermal conductivity
h_{con}	Interfacial convective heat transfer coefficient
T_{con}	Outside convection temperature
σ_s	Stefan-Boltzmann constant
ε	Emissivity
T_{rad}	Outside radiation temperature
L_{gas}	Latent heat of metal gasification
m	Molecular mass of the metal
k_B	Boltzmann's constant
P_0	Standard atmospheric pressure
T_{gas}	Metal gasification temperature
p	Pressure
$\boldsymbol{\tau}$	Stress tensor
$\overline{\mu}$	Mixed viscosity
$\mathbf{I}$	Unit matrix
$\boldsymbol{g}$	Acceleration of gravity
K_C	Drag coefficient of the mushy zone[42]
f_{liquid}	Liquid-phase fraction
C_K	A custom smaller value, such as 10^{-6}, used to prevent the drag force of the mushy zone from becoming infinite during the calculation (when f_{liquid} is zero)
σ	Surface tension coefficient
$\frac{d\sigma}{dT}$	Temperature coefficient of surface tension
κ	Interface curvature
$\boldsymbol{n}$	Unit normal vector on the interface

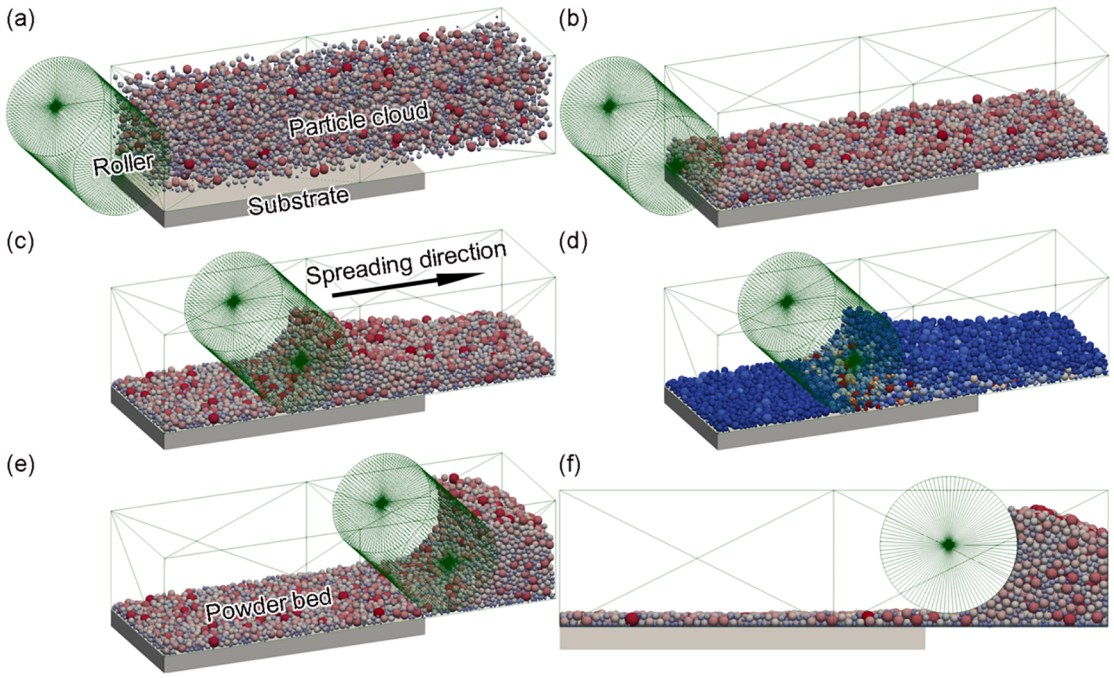

Fig. 1. Computation flow of spreading powder process: (a) generating a cloud of particles; (b) particles falling and accumulating on top of the substrate; (c) spreading powder in progress; (d) shear stress on particles; (e) spreading powder finish (three-dimensional view); (f) spreading powder finish (side view).

evolution during the SLM process by setting equivalent physical parameters and flow behavior models [30]. Ramos *et al.* [31] predicted the stress distributions under three scanning strategies (unidirectional, zigzag, and alternating) based on the macroscopic scale, and found that scanning strategy alternating was effective in reducing residual stresses and deformations. The most important part of the SLM process is the melting and solidification of the metal particles by laser heating, which is neglected in the macro-scale description of the SLM process. The idea of meso-scale simulation is to directly calculate the heating and melting action of laser on metal particles by geometrical modeling based on the particle shape, and then to describe the complex dynamic behavior of the mesoscopic molten pool [32,33]. The main factors of interest in meso-scale simulation studies are particle size distribution [34,35], layer thickness [36], laser power [37,38], scanning speed [39], and

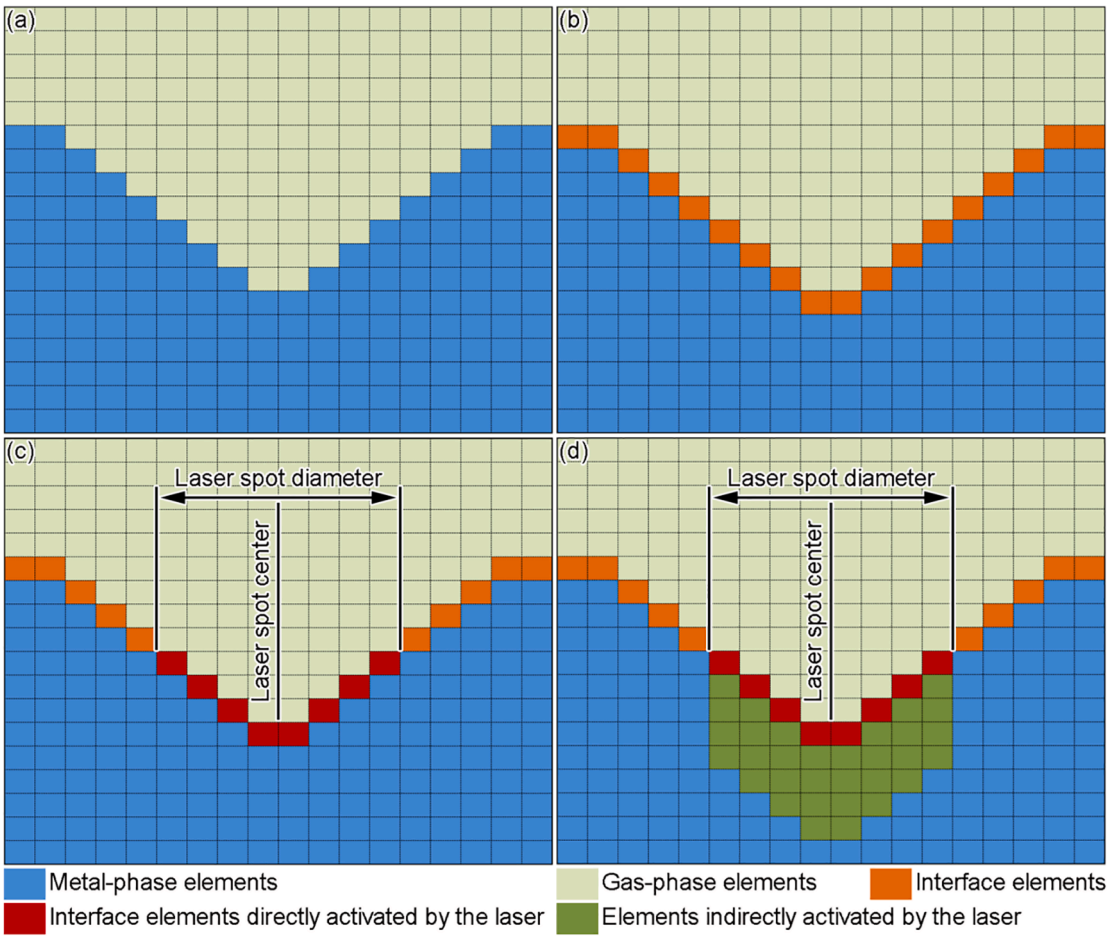

Fig. 2. Diagram of laser heat source model: (a) labeled metal-phase and gas-phase elements; (b) labeled interface elements; (c) labeled elements directly activated by the laser; (d) labeled elements indirectly activated by the laser.

hatch space [40]. No mesoscopic-scale simulation studies have been reported on the influences of scanning strategies on the SLM processes, which is the focus of this paper.

Based on the open-source discrete element method framework Yade and the open-source finite volume method framework OpenFOAM, the SLM mesoscopic molten pool dynamics behavior was predicted here. In order to analyze the influences of different scanning strategies on the SLM process, a simulation flow of SLM multi-layer multi-path forming process at the mesoscopic scale was established. The influences of different scanning strategies on grain orientation, pore defect and surface roughness were analyzed and compared with the experimental results. This paper is expected to provide a basis for the selection of scanning strategies in practical SLM production.

2. Mesoscopic-scale model of SLM

2.1. Particle distribution of powder bed

Describing the SLM process based on the mesoscopic scale requires the particle distribution of the powder bed first. The open-source discrete element method (DEM) framework Yade [33] was used to predict the spreading powder process. Fig. 1 shows the computation flow of the spreading powder process, which consists of the following four main steps: (1) the metal particles were treated as elastic spheres with contact friction, and a loose cloud of particles of a certain size distribution was generated in a certain space above the substrate (Fig. 1a); (2) the particle cloud fell by gravity and accumulated above the substrate (Fig. 1b); (3) the roller was moved in the direction of spreading powder (Fig. 1c), during which the interactions of the roller with the particles and between the particles and the particles were taken into account (Fig. 1d); (4) after the roller moved a certain distance and the spreading powder process was finished, the radius and sphere center coordinates of the particles above the substrate were exported (Fig. 1e, f).

2.2. Mesoscopic-scale molten pool dynamics model

A proper laser heat source model is crucial for SLM mesoscopic-scale simulation studies, and the laser energy applied here was calculated as follows: (1) the VOF model [41] (Eqs. (1) and (2)) was used to characterize the volume fraction distribution of the metal and gas phases of the element (Fig. 2a); (2) the metal-phase elements at the interface were marked based on the volume fraction distribution of the metal and gas phases (Fig. 2b); (3) the interface elements directly activated by the laser were marked by the laser spot center and diameter (Fig. 2c); (4) the interface elements directly activated by the laser were used as starting points to find the elements within a certain distance along the direction of gravity, which were marked as the elements indirectly activated by the laser (Fig. 2d); (5) it is considered here that the laser energy was absorbed by the elements directly and indirectly activated by the laser, and the laser energy of a localized horizontal region was absorbed by the elements activated by the laser under that localized horizontal region. The distribution coefficient was calculated by Eq. (3), and the laser surface energy density at the location of each element activated by the laser was calculated by Eq. (4), which leaded to the laser body energy density (Eq. (5)).

$$\frac{\partial \alpha_1}{\partial t} + \nabla \cdot (\alpha_1 \boldsymbol{u}) = 0 \tag{1}$$

$$\alpha_1 + \alpha_2 = 1 \tag{2}$$

$$f_{metal} = \frac{V_{metal}}{V_{sum}} \tag{3}$$

$$q_{laser} = \frac{2\eta P_{laser}}{\pi R^2} exp\left(-2\frac{(x - x_0 - v_{laser}t)^2 + (y - y_0)^2}{R^2} \right) \tag{4}$$

$$Q_{laser} = f_{metal} \cdot \frac{q_{laser}}{\Delta z} \tag{5}$$

Once the laser heat source model was obtained, a computational fluid dynamics (CFD) model could be built to describe the SLM mesoscopic melt pool dynamics behavior. In order to ensure the efficiency of the numerical solution, the following two assumptions were made: the flow of liquid metal and gas were considered as laminar flows of incompressible Newtonian fluids, and the mass loss due to metal gasification was not taken into account. The effects of gasification recoil, Marangoni effect, surface tension, and mushy zone drag on the flow behavior of the SLM molten pool were considered herein, and the mesoscopic molten pool dynamics model developed was as follows:

(1) Energy equation [34]

$$\frac{\partial \overline{\rho} \overline{c}_e T}{\partial t} + \nabla \cdot \left(\overline{\rho} \boldsymbol{u} \overline{c}_e T \right) = \nabla \cdot \left(\overline{k} \nabla T \right) + Q_{laser} - |\nabla \alpha_1| \frac{2\overline{\rho} \overline{c}_e}{\rho_1 c_1 + \rho_2 c_2} \left\{ h_{con}(T - T_{con}) + \sigma_s \varepsilon \left(T^4 - T_{rad}^4 \right) + 0.82 \frac{L_{gas} m}{\sqrt{2\pi m k_B T}} P_0 exp\left[\frac{L_{gas} m}{k_B} \left(\frac{1}{T_{gas}} - \frac{1}{T} \right) \right] \right\} \tag{6}$$

$$\overline{\rho} = \alpha_1 \rho_1 + \alpha_2 \rho_2 \tag{7}$$

(2) Momentum equation

$$\frac{\partial \overline{\rho} \boldsymbol{u}}{\partial t} + \nabla \cdot (\overline{\rho} \boldsymbol{u} \otimes \boldsymbol{u}) = -\nabla p + \nabla \cdot \boldsymbol{\tau} + \overline{\rho} \boldsymbol{g} - \overline{\rho} K_C \left[\frac{(1 - f_{liquid})^2}{f_{liquid}^3 + C_K} \right] \boldsymbol{u} + \left\{ \sigma \kappa \boldsymbol{n} + \frac{d\sigma}{dT} [\nabla T - \boldsymbol{n}(\boldsymbol{n} \cdot \nabla T)] + 0.54 P_0 exp\left[\frac{L_{gas} m}{k_B} \left(\frac{1}{T_{gas}} - \frac{1}{T} \right) \right] \boldsymbol{n} \right\} |\nabla \alpha_1| \tag{8}$$

$$\boldsymbol{\tau} = 2\overline{\mu} \left[\left(\frac{1}{2} \nabla \boldsymbol{u} + \frac{1}{2} (\nabla \boldsymbol{u})^T \right) - \frac{1}{3} (\nabla \cdot \boldsymbol{u}) \mathbf{I} \right] \tag{9}$$

$$\boldsymbol{n} = \frac{\nabla \alpha_1}{|\nabla \alpha_1|} \tag{10}$$

$$\kappa = -\nabla \cdot \boldsymbol{n} \tag{11}$$

(3) Continuity equation

$$\nabla \cdot \boldsymbol{u} = 0 \tag{12}$$

2.3. Simulation flow considering the influence of scanning strategy on SLM process

In this paper, the spreading powder process was calculated based on the open-source DEM framework Yade and the SLM mesoscopic molten pool dynamics behavior was predicted based on the open-source finite volume method (FVM) framework OpenFOAM [34,37,40]. In order to analyze the influence of different scanning strategies on the SLM process, it is necessary to calculate the multi-layer multi-path forming process, and Fig. 3 shows the simulation flow herein. The steps of this simulation process include: (1) the particle size distribution of metal powders was obtained by experimental means (e.g. particle size analyzers) or literature data (Fig. 3a); (2) the particle distribution of the first powder bed was obtained based on Yade, and the radius and sphere center coordinates of the powder bed particles were derived (Fig. 3b); (3) the forming process of the first layer powder bed was predicted based on OpenFOAM and the result was exported in STL format (Fig. 3c); (4) the STL file was imported into Yade to obtain the particle distribution of the second powder bed and export the radius and sphere center coordinates of the powder bed particles (Fig. 3d); (5) the forming process of the second layer powder bed was predicted based on OpenFOAM and the result was exported in STL format (Fig. 3e); (6) steps (4, 5) were repeated to form the subsequent powder bed.

3. Results and discussion

3.1. Calculation parameters

Based on the above simulation flow, the numerical simulation study of the SLM process at the mesoscopic scale was carried out here. The alloy used was 316L stainless steel with the following composition (percentage by mass): Fe 65.395%-Cr 17.0%-Ni 12.0%-Mo 2.5%-Mn 2.0%-Si 1.0%-P 0.045%-C 0.03%-S 0.03%. The particle size distribution of the powder satisfied a Gaussian distribution (central value of 25 μm and variance of 7.5 μm) and was artificially controlled between 10 μm and 40 μm. When predicting the spreading powder process based on Yade, the material parameters set include Young's modulus (195 GPa), density (7270 kg/m^3), Poisson's ratio (0.3), and contact friction angle (0.1). When predicting the dynamic behavior of SLM molten pool based on OpenFOAM, the material parameters to be set are shown in Table 1, which were calculated by the software JMatPro v7.0.

The interest here is the influence of scanning strategies on the SLM process based on mesoscopic-scale analysis, and the scanning strategies used include: One-direction, Two-directions, and Pre-sinter, which are schematically shown in Fig. 4. The scanning direction of scanning strategy One-direction was always kept in the X-axis and the scanning directions of adjacent scanning paths within the same forming layer were reversed. The scanning direction of scanning strategy Two-directions alternated between X and Y axes as the number of forming layer increased, and the scanning directions of adjacent scanning paths within the same forming layer were reversed. The scanning direction of scanning strategy Pre-sinter was the same as scanning strategy One-direction, but each scanning path was subjected to two laser actions (preheating before forming). To compare the influences of different scanning strategies on the SLM process, the SLM process parameters used here were kept constant, as shown in Table 2. Considering the heavy calculation burden of SLM simulation studies at the mesoscopic scale, in order to reasonably control the calculation cost, the forming processes of the first two powder layers for each of the three scanning strategies mentioned above were predicted, and the geometries of the calculation domains are: X-direction (800 μm), Y-direction (450 μm), and Z-direction (190 μm). In addition, the mesh cell size was 2.5 μm, the calculation time step was 5×10^{-7} s, the laser absorptivity was 0.35, the ambient temperature was 300 K, and the computing resources used were

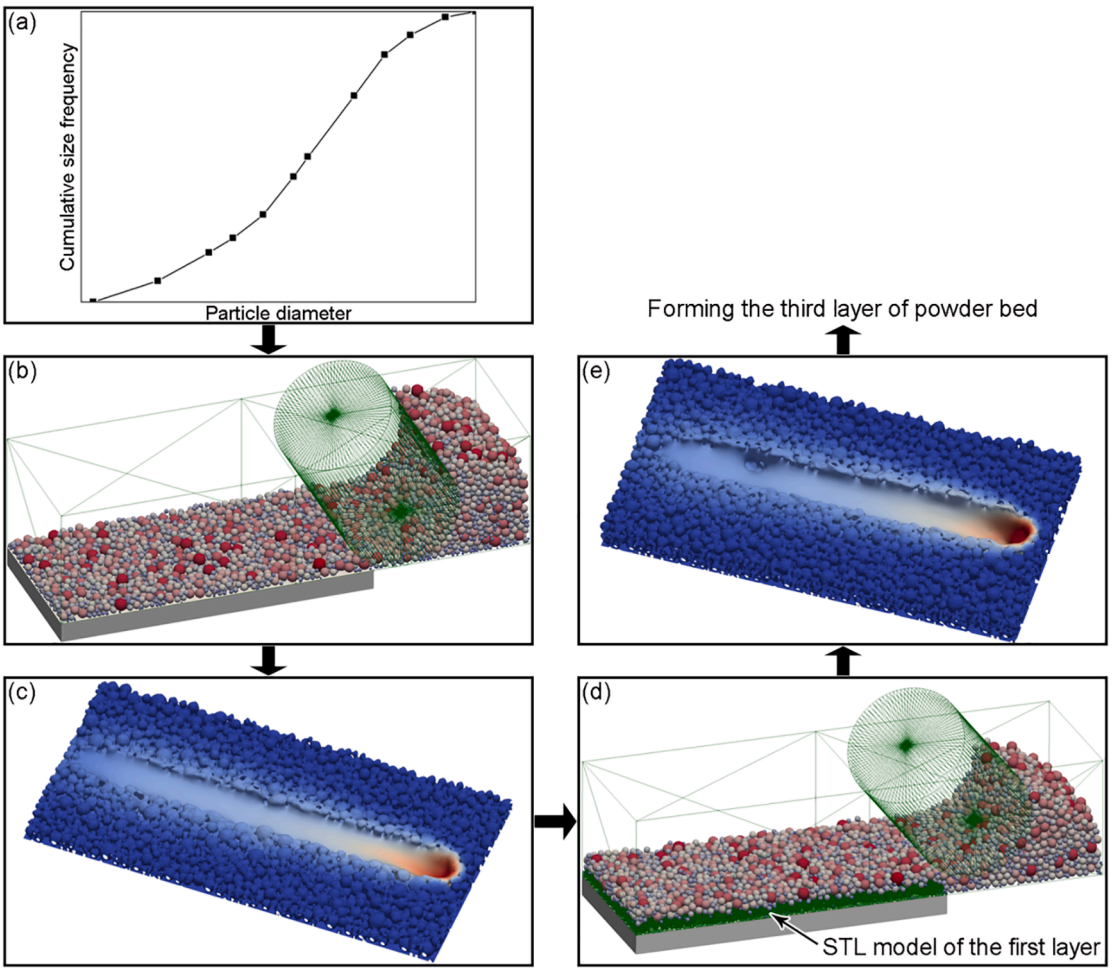

Fig. 3. Simulation flow considering the influence of scanning strategy on SLM process: (a) particle size distribution; (b) predicting the first powder layer; (c) forming the first powder layer; (d) predicting the second powder layer; (e) forming the second powder layer.

Intel Xeon Gold 6240 CPU (dual CPU, 72 threads, 128 GB memory).

3.2. *Influence of scanning strategy on grain orientation*

Fig. 5 shows the temperature distributions of the first two layers of the powder bed when formed with different scanning strategies. From the results, it can be seen that the metal particles melted rapidly under the action of the laser, forming a molten pool, and as the laser remained mobile, the superheated molten pool conducted heat to the adjacent metal and gas phases, which in turn solidified to form a solidified track. Taking the center of the laser spot as the origin, it can be considered that the molten pool state remained quasi-steady during the forming process, and the molten pool morphology was approximately teardrop-shaped. Since the distinguishing features of the SLM solidification process were epitaxial crystallization and selective growth, the molten pool boundaries during the forming process dominated the grain orientation. Fig. 6 shows the cross-sections (x = 400 μm) of the molten pool when forming each path of each layer under scanning strategy One-direction, where the criterion for selecting an image was the moment when the lower boundary of the molten pool was at its lowest position. Because the molten pool boundaries in Fig. 6 could be thought of as the starting points for subsequent grain growth to form the solidified tracks, so they could represent the solidified track boundaries. From the results of Fig. 6, it can be seen that the lower boundary of each molten pool was concave, so the grains of each solidified track would start from the lower boundary of the molten pool and grow perpendicularly to the liquid–solid interface.

To further analyze the influence of the scanning strategy on grain orientation, Fig. 7 presents the cross-sections of formed zones obtained for the first two layers of the powder bed under different scanning strategies. To show where the boundaries of each solidified track were located, the molten pool boundaries under each scanning strategy were

Table 1
Material parameters needed to predict the dynamic behavior of molten pool.

Parameter	Value	Unit
Density of metal	7270	kg/m^3
Specific heat of metal	790	J/(kg·K)
Thermal conductivity of metal	24.55	W/(m·K)
Solidus temperature	1658	K
Liquidus temperature	1723	K
Evaporation temperature	3090	K
Latent heat of melting	2.7×10^5	J/kg
Latent heat of gasification	7.45×10^6	J/kg
Viscosity of liquid metal	0.00345	Pa·s
Surface tension	1.6	N/m
Temperature coefficient of surface tension	-8×10^{-4}	N/(m·K)
Molecular mass	9.3×10^{-26}	kg
Ambient pressure	101,325	Pa
Boltzmann constant	1.380649×10^{-23}	J/K
Emissivity	0.26	
Stefan-Boltzmann constant	5.67×10^{-8}	$W/(m^2 \cdot K^4)$
Density of air	1	kg/m^3
Specific heat of air	718	J/(kg·K)
Thermal conductivity of air	0.02346	W/(m·K)
Viscosity of air	1.48×10^{-5}	Pa·s

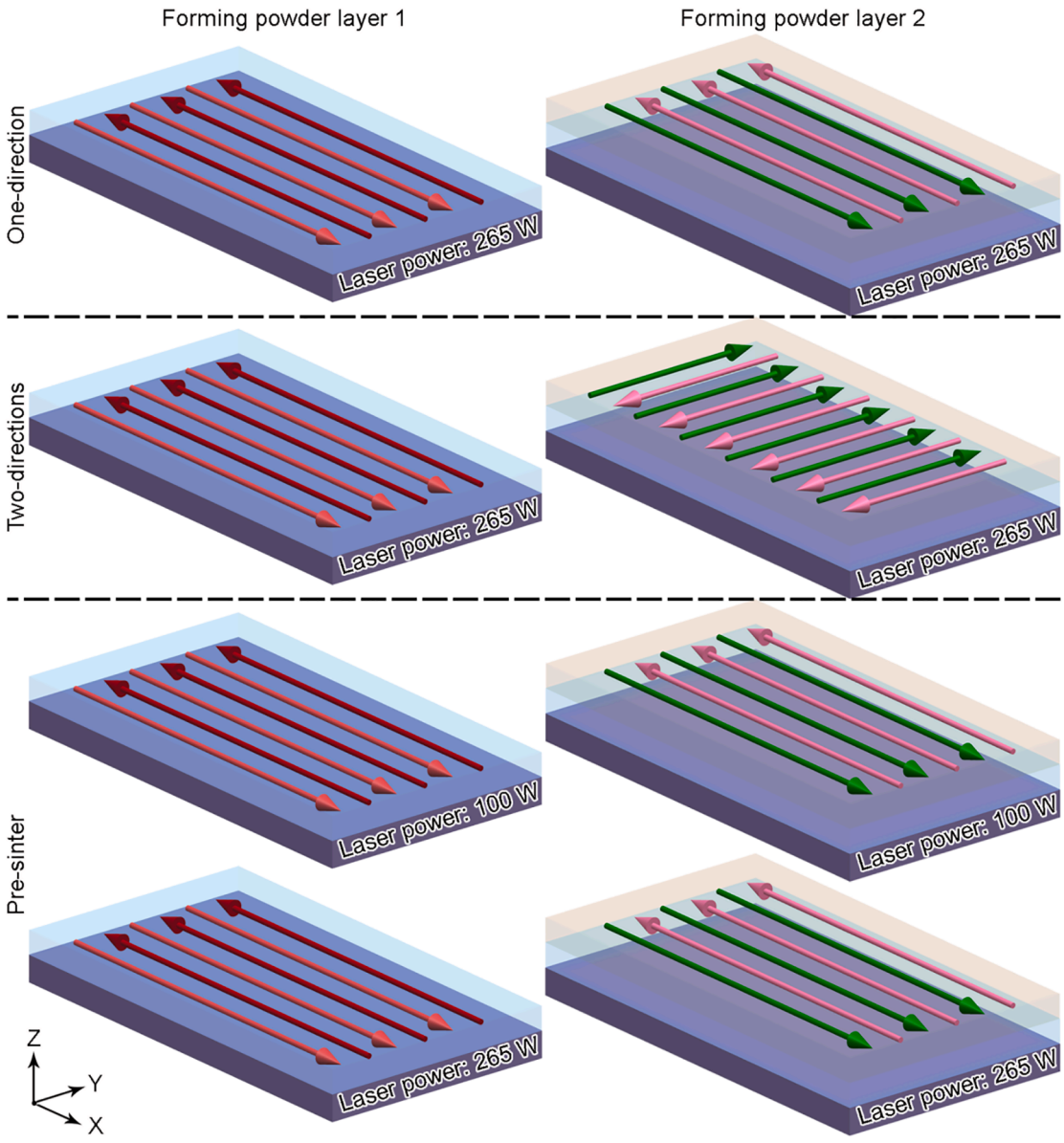

Fig. 4. Diagram of the scanning strategies.

Table 2
SLM process parameters.

Parameter	Value	Unit
Spot diameter	70	μm
Layer thickness	45	μm
Hatch space	60	μm
Scanning speed	1	m/s
Laser power (forming)	265	W
Laser power (preheat)	100	W

extracted here (Fig. 6 shows the molten pool boundaries under scanning strategy One-direction), and were identified by yellow curves in Fig. 7. For scanning strategy One-direction, since the scanning directions of adjacent formed layers were parallel to each other, it could be assumed that the solidified tracks of the current formed layer were stacked along the solidified tracks of the previous formed layer, so that the grain orientation of the current formed layer was essentially the same as that of the previous layer (Fig. 8a). For scanning strategy Two-directions, since the scanning directions of adjacent formed layers were perpendicular to each other, the solidified tracks of the current formed layer could be considered to be stacked perpendicular to the solidified tracks of the previous formed layer, resulting in the grain orientation of the current formed layer being significantly different from that of the previous layer (Fig. 8b). For scanning strategy Pre-sinter, the grain orientation of the formed layer was almost the same as scanning strategy One-direction, but since the powder bed needed to be preheated before forming, the grain size of scanning strategy Pre-sinter would be larger than that of scanning strategy One-direction. In summary, the grain orientation of the current formed layer under scanning strategies One-direction and Pre-sinter was almost the same as that of the previous layer, while the grain orientation of the current formed layer under scanning strategy Two-directions was significantly different from that of the previous layer.

3.3. *Influence of scanning strategy on pore defect*

Next, the influence of the scanning strategy on the pore defects was analyzed, and since each element in the calculation has parameter α_1 (metal-phase volume fraction), the porosity could be found by counting

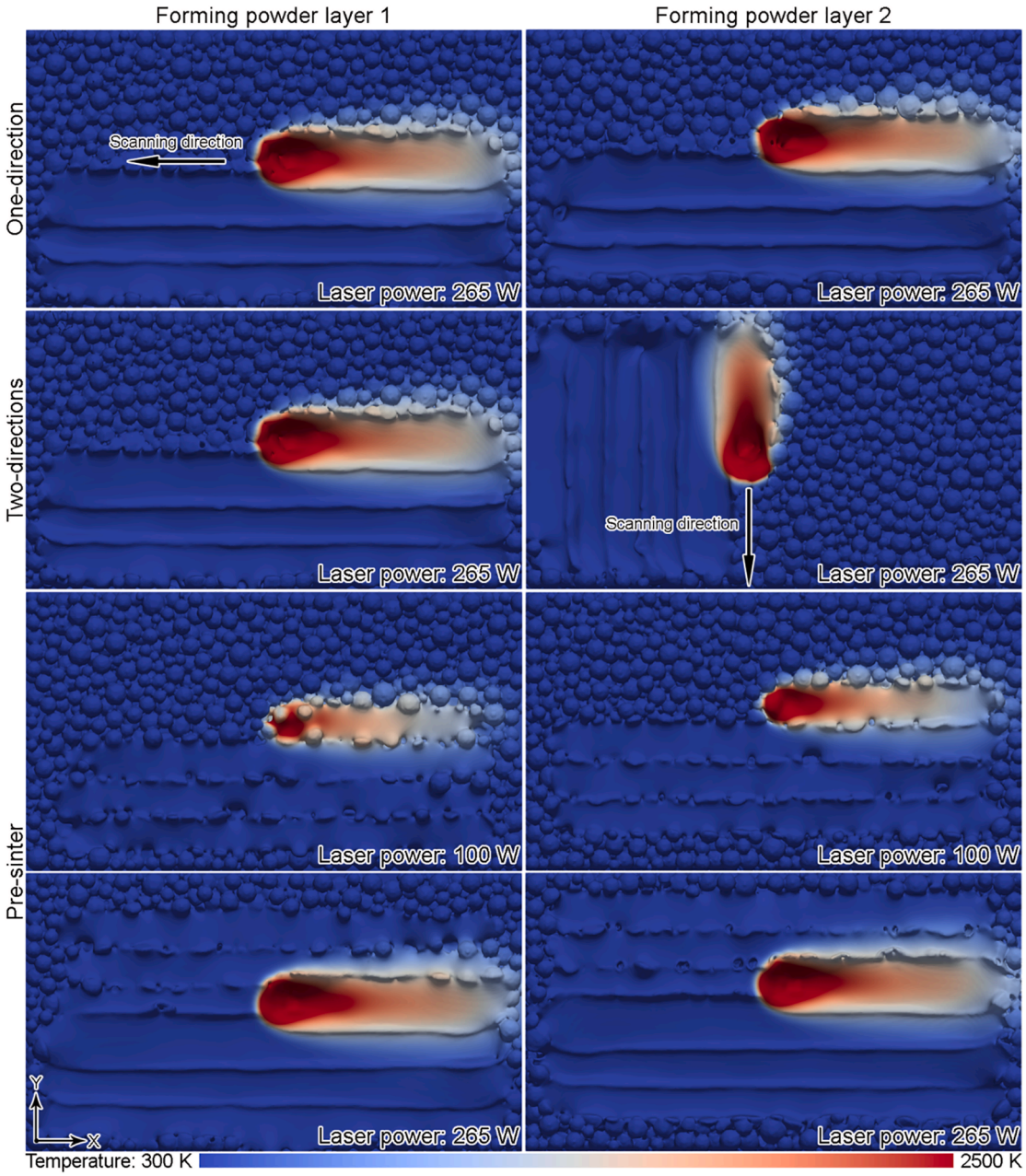

Fig. 5. Temperature distributions of the first two layers of the powder bed when formed with different scanning strategies.

the metal and gas phase volumes of each element. Fig. 9 shows the gas-solid interfaces of the final formed region with different scanning strategies, which is the contour surface of $\alpha_1 = 0.5$. It is obvious that there were pores inside the formed region, but since the laser did not act on the entire calculation domain during the forming process, it was inappropriate to directly count the gas-phase volume of the entire calculation domain. So, the local body region (Fig. 9) was selected here for calculating porosity, which avoided the powder bed region that was not subject to laser action. With the aid of the post-processing software ParaView v5.4.0, the gas-phase volumes of the local body regions under different scanning strategies were extracted, and the corresponding porosities were calculated, as shown in Table 3. From the porosity results, it can be seen that the porosity under scanning strategy Pre-sinter was significantly lower than that under scanning strategies One-direction and Two-directions. The same rule was obtained from the experimental results [22]. The reason for this rule is that, compared to scanning strategies One-direction and Two-directions, the powder bed under scanning strategy Pre-sinter needed to be preheated first, resulting in a certain degree of sintering (Fig. 5), which corresponded to already reduced interparticle voids. When high power lasers were used for forming, the heat was more easily transmitted between the metal particles, resulting in a deeper and wider molten pool, giving more time for the gas caught in the molten pool to escape, thus achieving a lower porosity. In summary, the relative density of part made under scanning strategy Pre-sinter is higher than that under scanning strategies One-direction and Two-directions.

3.4. *Influence of scanning strategy on surface roughness*

Finally, the influence of the scanning strategy on surface roughness was analyzed, and it is suggested here that the upper surface on Z-direction of the gas-solid interface in the final formed region could reflect the size of the surface roughness. Considering that the laser did not act on the entire calculation domain, a portion of the upper surface was

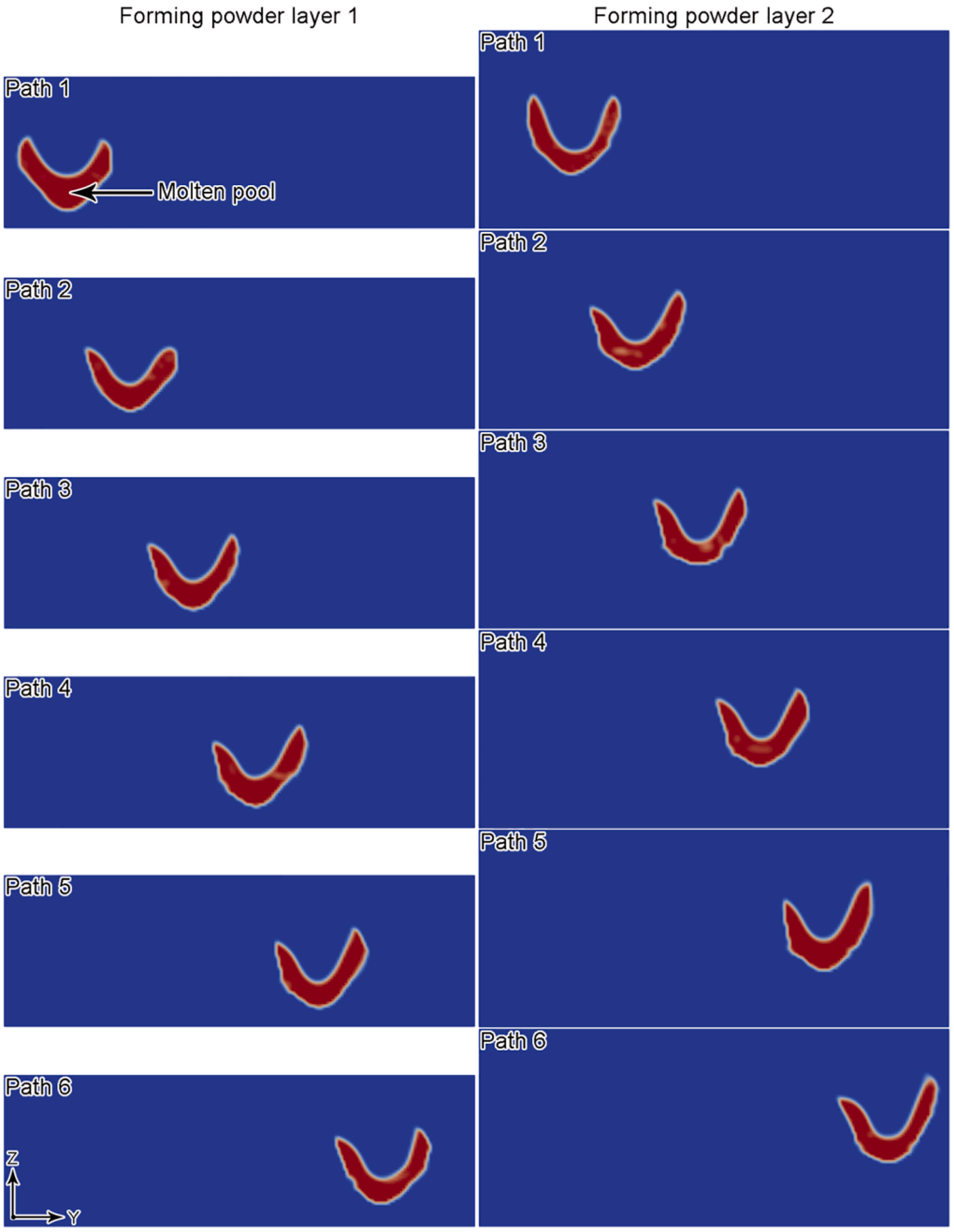

Fig. 6. Cross-sections (x = 400 μm) of the molten pool when forming each path of each layer under scanning strategy One-direction.

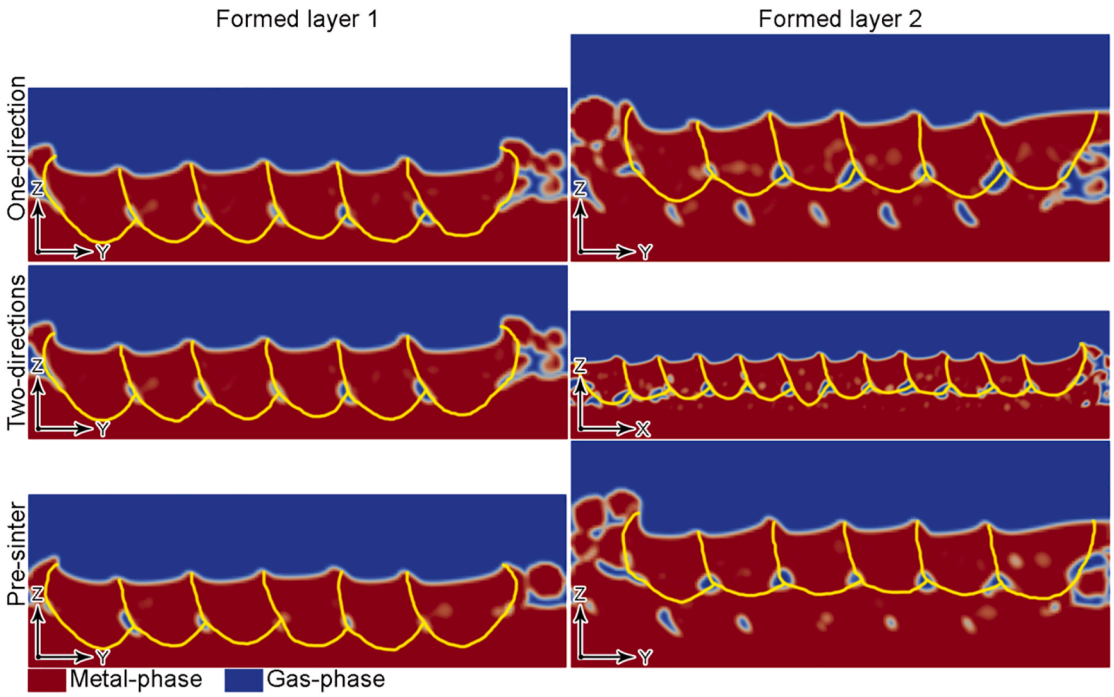

Fig. 7. Cross-sections of formed zones obtained for the first two layers of the powder bed under different scanning strategies (x = 400 μm, the yellow curves represent the molten pool boundaries obtained when forming each path).

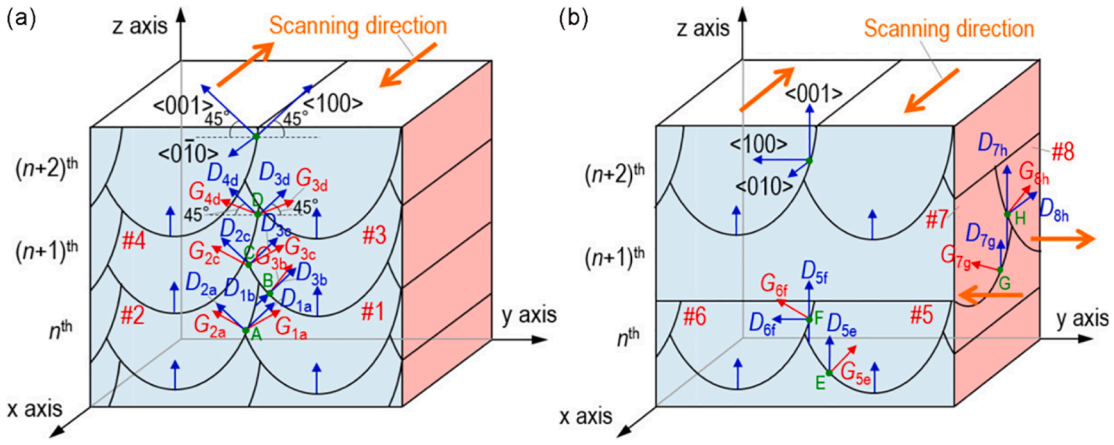

Fig. 8. Schematic diagram of solidified track boundaries and grain orientations for different scanning strategies [23]: (a) scanning strategy One-direction; (b) scanning strategy Two-directions.

extracted based on Fig. 9, as shown in Fig. 10. ParaView v5.4.0 can extract node information for local surface area, and the surface roughness can be calculated as follows:

$$z_{average} = \frac{\sum_{i=1}^{M} z_i}{M} \tag{13}$$

$$S_{roughness} = \frac{\sum_{i=1}^{M} \left| z_i - z_{average} \right|}{M} \tag{14}$$

where, z_i is the Z-directional height of the node; M is the number of nodes; $z_{average}$ is the average height of the nodes in the local surface area; $S_{roughness}$ is the surface roughness. It should be noted that the X-dimension of the extracted local surface area was only a few hundred microns, which differed greatly from the actual size of the part, so the so-called surface roughness data herein could only be considered as a mapping of the actual surface roughness of the part, and the specific value could not represent the actual surface roughness. z_i could be provided by ParaView v5.4.0, and the extracted surface roughness data for each scanning strategy can be seen in Table 4. From the surface roughness results, it can be seen that the surface roughness under scanning strategy Pre-sinter was significantly lower than that under scanning strategies One-direction and Two-directions. The reason for this is that, compared to scanning strategies One-direction and Two-directions, the powder bed under scanning strategy Pre-sinter needed to be preheated first, resulting in a certain degree of sintering (Fig. 5), which corresponded to a reduced degree of surface fluctuation of the powder bed already. When forming with high-powered laser, the deeper and wider molten pool facilitated a flattened solidified track, resulting in a lower surface roughness. In summary, the surface flatness of the fabricated part under scanning strategy Pre-sinter is better than that under scanning strategies One-direction and Two-directions.

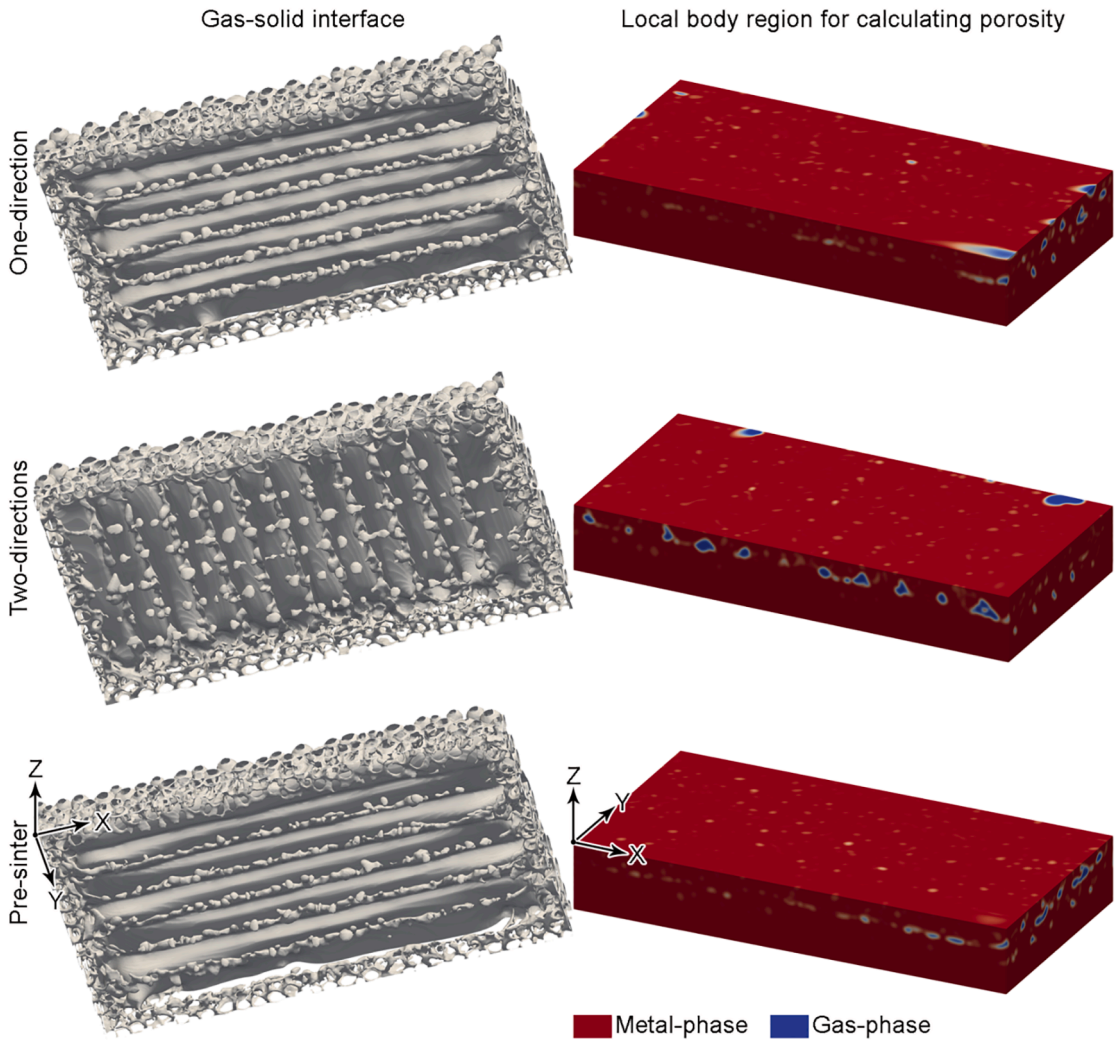

Fig. 9. Gas-solid interfaces in the final formed regions and local body regions for calculating porosity under different scanning strategies.

Table 3
Porosity under different scanning strategies.

Scanning strategy	Porosity (%)
One-direction	5.49
Two-directions	5.92
Pre-sinter	4.66

4. Conclusions

(1) The spreading powder process was calculated based on the open-source DEM framework Yade, and the SLM mesoscopic molten pool dynamics behavior was predicted based on the open-source FVM framework OpenFOAM. To analyze the influence of different scanning strategies (One-direction, Two-directions and Pre-sinter) on the SLM process, the simulation flow of SLM multi-layer multi-path forming process at the mesoscopic scale was developed.

(2) Regarding the influence of the scanning strategy on grain orientation, it was found that the grain orientation of the current formed layer under scanning strategies One-direction and Pre-sinter was almost the same as that of the previous layer, while the grain orientation of the current formed layer under scanning strategy Two-directions was significantly different from that of the previous layer.

(3) Regarding the influences of scanning strategy on porosity defect and surface roughness, it was found that porosity and surface roughness under scanning strategy Pre-sinter were lower than those under scanning strategies One-direction and Two-directions. This paper is expected to provide a basis for the selection of scanning strategies in practical SLM production.

CRediT authorship contribution statement

Liu Cao: Conceptualization, Data curation, Formal analysis, Funding acquisition, Investigation, Methodology, Project administration, Resources, Software, Supervision, Validation, Visualization, Writing - original draft, Writing - review & editing.

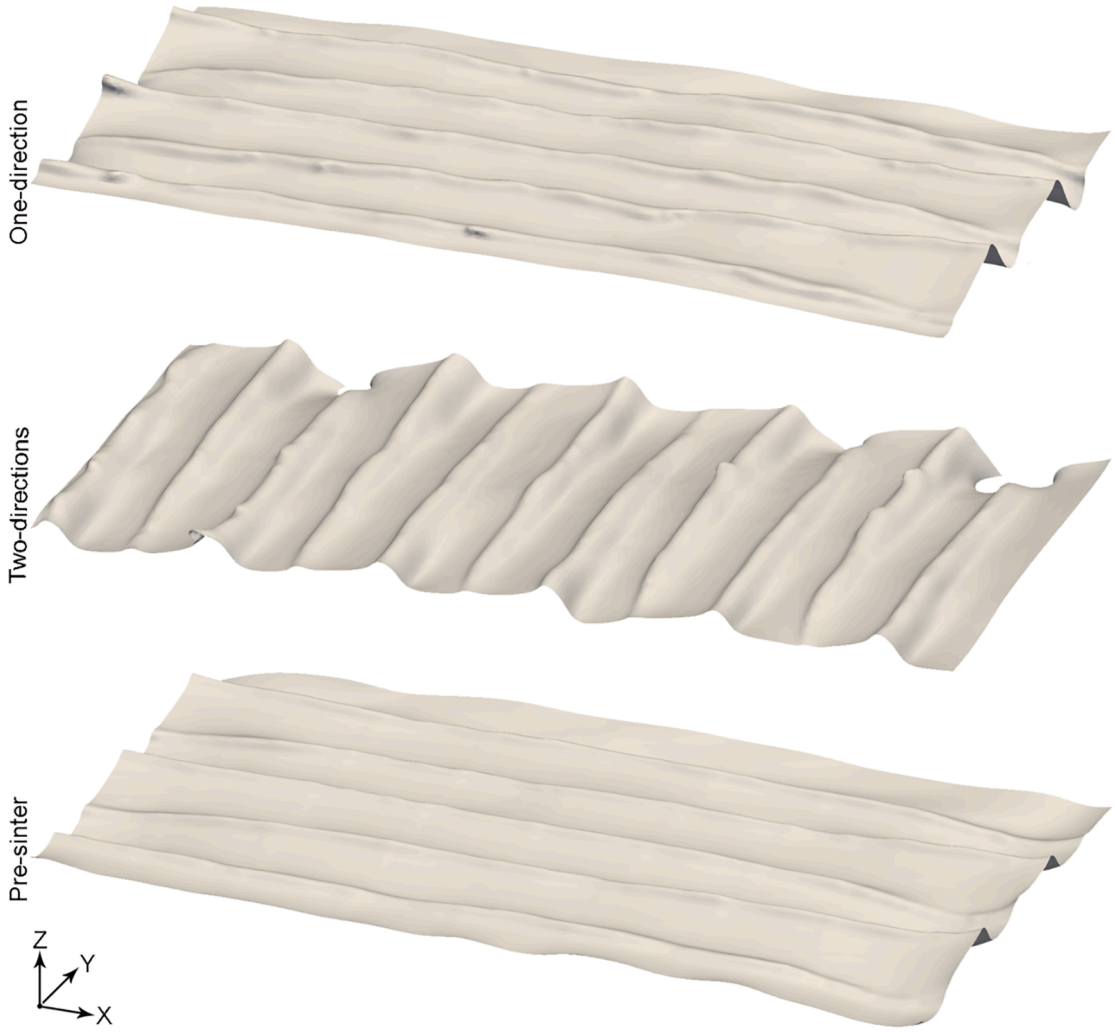

Fig.10. Local surface areas for calculating surface roughness under different scanning strategies.

Table 4
Surface roughness under different scanning strategies.

Scanning strategy	Surface roughness (μm)
One-direction	4.41
Two-directions	4.66
Pre-sinter	3.97

Declaration of Competing Interest

The authors declare that they have no known competing financial interests or personal relationships that could have appeared to influence the work reported in this paper.

Acknowledgement

This work was supported by the Natural Science Foundation of Guangdong Province (no. 2019A1515012040).

References

[1] W.-N. Zhang, L.-Z. Wang, Z.-X. Feng, Y.-M. Chen, Research progress on selective laser melting (SLM) of magnesium alloys: A review, Optik 207 (2020) 163842, https://doi.org/10.1016/j.ijleo.2019.163842.
[2] X. Zhang, C.J. Yocom, B.o. Mao, Y. Liao, Microstructure evolution during selective laser melting of metallic materials: A review, J. Laser Appl. 31 (3) (2019) 031201, https://doi.org/10.2351/1.5085206.
[3] Z.-C. Fang, Z.-L. Wu, C.-G. Huang, C.-W. Wu, Review on residual stress in selective laser melting additive manufacturing of alloy parts, Opt. Laser Technol. 129 (2020) 106283, https://doi.org/10.1016/j.optlastec.2020.106283.
[4] A. Ahmed, A. Majeed, Z. Atta, G.Z. Jia, Dimensional quality and distortion analysis of thin-walled alloy parts of AlSi10Mg manufactured by selective laser melting, J. Manuf. Mater. Process. 3 (2019) 51.
[5] J. Han, M. Wu, Y. Ge, J. Wu, Optimizing the structure accuracy by changing the scanning strategy using selective laser melting, Int. J. Adv. Manuf. Technol. 95 (9-12) (2018) 4439–4447, https://doi.org/10.1007/s00170-017-1503-7.
[6] S.D. Bagg, L.M. Sochalski-Kolbus, J.R. Bunn, The effect of laser scan strategy on distortion and residual stresses of arches made with selective laser melting, Proceedings of American Society for Precision Engineering Annual Meeting, 2016.
[7] D.D. Gu, M. Guo, H.M. Zhang, Y.X. Sun, R. Wang, L. Zhang, Effects of laser scanning strategies on selective laser melting of pure tungsten, Int. J. Extreme Manuf. 2 (2020) 025001.
[8] J. Han, Y. Ge, Y. Mao, M. Wu, A study on the surface quality of the 3D printed parts caused by the scanning strategy, Rapid Prototyping J. 25 (2) (2019) 247–254, https://doi.org/10.1108/RPJ-06-2017-0125.
[9] J. Han, M. Wu, Y. Ge, A study on the dimension accuracy on the inner structure of the 3D printed parts caused by the scanning strategy, Materials 12 (2019) 1333.
[10] J. Hajnys, M. Pagáč, J. Měsíček, J. Petru, M. Król, Influence of scanning strategy parameters on residual stress in the SLM process according to the bridge curvature method for AISI 316L stainless steel, Materials 13 (2020)1659.
[11] D. Wang, S.B. Wu, Y.Q. Yang, W.H. Dou, S.S. Deng, Z. Wang, S. Li, The effect of a scanning strategy on the residual stress of 316L steel parts fabricated by selective laser melting (SLM). Materials 11 (2018) 1821.
[12] H.Y. Wan, Z.J. Zhou, C.P. Li, G.F. Chen, G.P. Zhang, Effect of scanning strategy on grain structure and crystallographic texture of Inconel 718 processed by selective laser melting, J. Mater. Sci. Technol. 34 (10) (2018) 1799–1804, https://doi.org/10.1016/j.jmst.2018.02.002.
[13] L. Thijs, B. Vrancken, J.-P. Kruth, J.V. Humbeeck, The influence of process parameters and scanning strategy on the texture in Ti6Al4V parts produced by selective laser melting, J. Mater. Sci. Technol. 1 (2013) 21–28.

[14] H. Zhang, D. Gu, D. Dai, C. Ma, Y. Li, R. Peng, S. Li, G. Liu, B. Yang, Influence of scanning strategy and parameter on microstructural feature, residual stress and performance of Sc and Zr modified Al–Mg alloy produced by selective laser melting, Mater. Sci. Eng., A 788 (2020) 139593, https://doi.org/10.1016/j.msea.2020.139593.
[15] Y.C. Wang, L.M. Lei, L. Shi, H.Y. Wan, F. Liang, G.P. Zhang, Scanning strategy dependent tensile properties of selective laser melted GH4169, Mater. Sci. Eng., A 788 (2020) 139616, https://doi.org/10.1016/j.msea.2020.139616.
[16] H.Y. Wan, Z.J. Zhou, C.P. Li, G.F. Chen, G.P. Zhang, Effect of scanning strategy on mechanical properties of selective laser melted Inconel 718, Mater. Sci. Eng., A 753 (2019) 42–48, https://doi.org/10.1016/j.msea.2019.03.007.
[17] T. Larimian, M. Kannan, D. Grzesiak, B. AlMangour, T. Borkar, Effect of energy density and scanning strategy on densification, microstructure and mechanical properties of 316L stainless steel processed via selective laser melting, Mater. Sci. Eng., A 770 (2020) 138455, https://doi.org/10.1016/j.msea.2019.138455.
[18] O.O. Salman, F. Brenne, T. Niendorf, J. Eckert, K.G. Prashanth, T. He, S. Scudino, Impact of the scanning strategy on the mechanical behavior of 316L steel synthesized by selective laser melting, J. Manuf. Process. 45 (2019) 255–261, https://doi.org/10.1016/j.jmapro.2019.07.010.
[19] C.Y. Liu, J.D. Tong, M.G. Jiang, Z.W. Chen, G. Xu, H.B. Liao, P. Wang, X.Y. Wang, M. Xu, C.S. Lao, Effect of scanning strategy on microstructure and mechanical properties of selective laser melted reduced activation ferritic/martensitic steel, Mater. Sci. Eng., A 766 (2019) 138364, https://doi.org/10.1016/j.msea.2019.138364.
[20] H. Zhang, D. Gu, C. Ma, M. Guo, R. Wang, J. Yang, Q. Ge, Microstructure and tribological property of selective laser melted Ni-based composites using different scanning strategies, Vacuum 177 (2020) 109439, https://doi.org/10.1016/j.vacuum.2020.109439.
[21] E.H. Valente, C. Gundlach, T.L. Christiansen, M.A.J. Somers, Effect of scanning strategy during selective laser melting on surface topography, porosity, and microstructure of additively manufactured Ti-6Al-4V, Appl. Sci. 9 (2019) 5554.
[22] N.T. Aboulkhair, N.M. Everitt, I. Ashcroft, C. Tuck, Reducing porosity in AlSi10Mg parts processed by selective laser melting, Addit. Manuf. 1–4 (2014) 77–86.
[23] S.H. Sun, H. Koji, T. Nakano, Effect of scanning strategy on texture formation in Ni-25 at. %Mo alloys fabricated by selective laser melting, Mater. Design 140 (2018) 307–316.
[24] H. Kyogoku, T.-T. Ikeshoji, A review of metal additive manufacturing technologies: mechanism of defects formation and simulation of melting and solidification phenomena in laser powder bed fusion process, Mech. Eng. Rev. 7 (1) (2020) 19–00182.
[25] S.A. Khairallah, A.T. Anderson, A. Rubenchik, W.E. King, Laser powder-bed fusion additive manufacturing: Physics of complex melt flow and formation mechanisms of pores, spatter, and denudation zones, Acta Mater. 108 (2016) 36–45.
[26] A. Ahrari, K. Deb, S. Mohanty, J.H. Hattel, Multi-objective optimization of cellular scanning strategy in selective laser melting. Proc. IEEE Conf. 2017, doi:10.1109/CEC.2017.7969639.
[27] L. Parry, I.A. Ashcroft, R.D. Wildman, Understanding the effect of laser scan strategy on residual stress in selective laser melting through thermo-mechanical simulation, Addit. Manuf. 12 (2016) 1–15.
[28] B. Cheng, S. Shrestha, K. Chou, Stress and deformation evaluations of scanning strategy effect in selective laser melting, Addit. Manuf. 12 (2016) 240–251.
[29] S. Mohanty, C.C. Tutum, J.H. Hattel, Cellular scanning strategy for selective laser melting: Evolution of optimal grid-based scanning path & parametric approach to thermal homogeneity. Proceedings of SPIE, 2013, doi:10.1117/12.2004256.
[30] J. Song, W.H. Wu, L. Zhang, B.B. He, L. Lu, X.Q. Ni, Q.L. Long, G.L. Zhu, Role of scanning strategy on residual stress distribution in Ti-6Al-4V alloy prepared by selective laser melting, Optik 170 (2018) 342–352.
[31] D. Ramos, F. Belblidia, J. Sienz, New scanning strategy to reduce warpage in additive manufacturing, Addit. Manuf. 28 (2019) 554–564.
[32] B.Q. Liu, G. Fang, L.P. Lei, W. Liu, A new ray tracing heat source model for mesoscale CFD simulation of selective laser melting (SLM), Appl. Math. Model. 79 (2020) 506–520.
[33] L. Cao, Study on the numerical simulation of laying powder for selective laser melting process, Int. J. Adv. Manuf. Technol. 105 (2019) 2253–2269.
[34] L. Cao, Numerical simulation of the impact of laying powder on selective laser melting single-pass formation, Int. J. Heat Mass Tran. 141 (2019) 1036–1048.
[35] D.D. Gu, M.J. Xia, D.H. Dai, On the role of powder flow behavior in fluid thermodynamics and laser processability of Ni-based composites by selective laser melting, Int. J. Mach. Tool. Manu. 137 (2019) 67–78.
[36] Z.K. Wang, W.T. Yan, W.K. Liu, M.B. Liu, Powder-scale multi-physics modeling of multi-layer multi-track selective laser melting with sharp interface capturing method, Comput. Mech. 63 (2019) 649–661.
[37] L. Cao, Mesoscopic-scale simulation of pore evolution during laser powder bed fusion process, Comp. Mater. Sci. 179 (2020), 109686.
[38] C. Tang, J.L. Tan, C.H. Wong, A numerical investigation on the physical mechanisms of single track defects in selective laser melting, Int. J. Heat Mass Tran. 126 (2018) 957–968.
[39] C. Panwisawas, C.L. Qiu, M.J. Anderson, Y. Sovani, R.P. Turner, M.M. Attallah, J. W. Brooks, H.C. Basoalto, Mesoscale modelling of selective laser melting: Thermal fluid dynamics and microstructural evolution, Comp. Mater. Sci. 126 (2017) 479–490.
[40] L. Cao, Mesoscopic-scale numerical simulation including the influence of process parameters on SLM single-layer multi-pass formation, Metall. Mater. Trans. A 51 (2020) 4130–4145.
[41] L. Cao, D.M. Liao, F. Sun, T. Chen, Z.H. Teng, Y.L. Tang, Prediction of gas entrapment defects during zinc alloy high-pressure die casting based on gas-liquid multiphase flow model, Int. J. Adv. Manuf. Technol. 94 (1) (2018) 807–815.
[42] L. Cao, F. Sun, T. Chen, Z.H. Teng, Y.L. Tang, D.M. Liao, Numerical simulation of liquid-solid conversion affecting flow behavior during casting filling process, Acta Metall. Sin. 53 (11) (2017) 1521–1531.